

# Chapter 5

## Electrically Tunable Filters based on Waveguide Gratings

*This chapter begins with a brief introduction into the theoretical description of waveguides and waveguide gratings. Furthermore, the potential of electrically controlled diffraction from Bragg waveguide gratings for the application as electrically tunable optical filters is explained. In addition, the process of fabrication of gratings in waveguides is discussed in detail. However, this discussion is restricted to two types of gratings: Photorefractive and Photolithographic. The implementation of the electrical control of diffraction from waveguide gratings in  $\text{LiNbO}_3$  is also presented. A detailed study on nonlinear properties of photorefractive gratings is included at the end of this chapter.*

### 5.1 Introduction

After the successful demonstration of the electrical control of diffraction for volume gratings in a bulk crystal (as discussed in chapter 4) and in view of the limitation proposed in section 4.8, the concept of electrical control of diffraction from Bragg gratings was implemented to integrated optical dimensions. In this case, the Bragg grating was realized in a waveguide and the transfer function was tuned using the external electric field. The term transfer function is used to describe the spectral dependence of diffraction efficiency and it contains information about the amplitude and phase-modulations of the original grating. This function can be obtained by illuminating the grating with the tunable read-out source and measuring the transmitted or the reflected signal as a function of the wavelength. The integrated optical implementation gives the advantage of miniaturization, faster switching or tuning due to reduced dimensions, lower voltage requirement and direct use within fiber optic systems without much insertion loss. Such electrically controllable Bragg gratings in waveguides exhibit narrow bandwidth and fast tuning and thus can be used as tun-

able optical filters for a range of applications such as DWDM (dense wavelength division multiplexing) telecommunication systems, spectroscopy, optical sensors, tunable lasers etc.

Before moving on to explain the theory and the procedure of the realization of electrically tunable integrated optical filters based on waveguide Bragg gratings as proposed above, it is important to consider the motivation for this study. With the growth of high-speed, high-capacity DWDM [51] optical communication systems, there is an ever increasing demand for faster speeds, more bandwidth and reduction of the spacing between the neighboring channels. Therefore, faster tunable optical filters with narrower bandwidth and steeper edges of the filter transfer function (which is defined as spectral response of the filter for transmitted or reflected light) are a continual necessity. Tunable optical filters based on different physical principles are already available. Fiber based filters such as fiber bragg gratings [9] (FBGs) and Fabry Perot [10] are the most commercialized. For high demanding dynamics, micromachined [11] and acousto-optic [12] filters offer a good solution in the microsecond tuning range. For the next-generation ultra-high speed requirements in the nanosecond range, faster mechanisms are needed such as the electro-optic effect. Thus, it is useful to study and innovate new designs for electrically tunable integrated optical filters which can be useful for various applications stated above.

## 5.2 Optical Waveguide Theory

An optical waveguide is the basic element in integrated photonics technology. This section seeks to introduce the basic theory of optical waveguides, before moving on to the realization of gratings in the waveguide. For further details, the reader is referred to several excellent texts such as [52–54] which are devoted to the subject of guided wave optics. An optical waveguide is a structure that allows the confinement of light within its boundaries by total internal reflection. It is the fundamental element that interconnects various elements of an integrated optical circuit, just like a metallic strip in an electrical integrated circuit. However, unlike electrical current that flows through a metal strip, optical waves travel in the waveguide in distinct optical modes. An optical mode is the transversal distribution of an electromagnetic field of the radiation that remains constant in time and is maintained as the light beam propagates through the waveguide. Depending on the type, profile, size, material, and the operational wavelength, a waveguide can support a single or multiple modes and is classified as single-mode or multi-mode waveguide, respectively. However, all the modes have discrete propagation constants and are mutually orthogonal.

Mathematically, a dielectric waveguide structure is completely specified by the refractive index profile  $n = n(\mathbf{r})$  and a mode is an electromagnetic field which is a solution of Maxwell's wave equation in the defined profile. A simple case of a planar waveguide ( $n = n(x)$ ) is considered as shown in Fig. 5.1. In order to find the propagating modes, two situations are considered: the electric field associated with the mode has only a transversal component (TE modes); the electric field has only a parallel component (TM modes). For TE

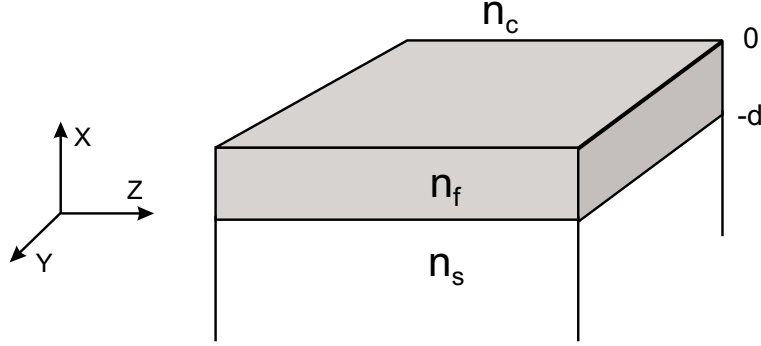


Figure 5.1: Geometry of an asymmetric planar waveguide

propagation, the electric field amplitude  $E_y(x)$  must satisfy the differential wave equation

$$\frac{d^2 E_y(x)}{dx^2} + [k_0^2 n^2(x) - \beta^2] E_y(x) = 0 \quad (5.1)$$

where  $k_0 = 2\pi/\lambda_0$  is the free-space propagation wave vector for the light wave with wavelength  $\lambda_0$  and  $\beta$  is the propagation constant of the mode. A general solution for the  $E_y(x)$  component in the above mentioned differential equation can be postulated in the form:

$$E_j(x) = A_j e^{i\gamma_j x} + B_j e^{-i\gamma_j x} \quad (5.2)$$

where  $E_j(x)$  represents the y-component of the electric field amplitude for the wave propagating in the  $j^{\text{th}}$  region,  $A_j$  and  $B_j$  are the two complex constants which will be calculated after imposing the appropriate boundary conditions. Eqn. (5.2) satisfied the wave equation (5.1), provided

$$\gamma_j = \sqrt{k_0^2 n_j^2 - \beta^2} \quad (5.3)$$

where  $\gamma_j$  is different for each region, characterized by its refractive index  $n_j$ .

In order to find the guided TE modes of the step-index asymmetric planar waveguides as shown in Fig. 5.1, the propagation constant  $\beta$  associated with a particular mode must fulfill the condition:

$$k_0 n_s < \beta < k_0 n_f \quad (5.4)$$

Keeping this in mind, the wave equation (5.1) in each homogeneous region of the waveguide can be written as

$$d^2 E_y/dx^2 - \gamma_c^2 E_y = 0 \quad x \geq 0 \quad (\text{Cover}) \quad (5.5)$$

$$d^2 E_y/dx^2 - k_f^2 E_y = 0 \quad 0 > x > -d \quad (\text{Film}) \quad (5.6)$$

$$d^2 E_y/dx^2 - \gamma_s^2 E_y = 0 \quad x \leq -d \quad (\text{Substrate}) \quad (5.7)$$

where the three parameters  $\gamma_c$ ,  $k_f$ , and  $\gamma_s$  are given by:

$$\gamma_c^2 = \beta^2 - k_0^2 n_c^2 \quad (5.8)$$

$$k_f^2 = k_0^2 n_f^2 - \beta^2 \quad (5.9)$$

$$\gamma_s^2 = \beta^2 - k_0^2 n_s^2 \quad (5.10)$$

By solving the differential equations (5.5)-(5.7) alongwith the boundary (continuity) conditions, a transcendental equation including the parameters that define the waveguide structure ( $n_c$ ,  $n_f$ ,  $n_s$  and  $d$ ), the working wavelength  $\lambda$  and the propagation constant  $\beta$  of the guided mode is obtained. From this transcendental equation, the propagation constant  $\beta$  is numerically calculated and with this, the coefficients  $\gamma_c$ ,  $k_f$  and  $\gamma_s$  are easily calculated, and thus the electric field in the three regions is completely determined:

$$E_y(x) = \begin{cases} Ae^{-\gamma_c x} & x \geq 0 \\ A \left( \cos k_f x - \frac{\gamma_c}{k_f} \sin k_f x \right) & 0 < x < -d \\ A \left( \cos k_f d + \frac{\gamma_c}{k_f} \sin k_f d \right) e^{\gamma_s(x+d)} & x \leq -d \end{cases} \quad (5.11)$$

According to this expression, the electric field decreases exponentially in the cover and in the substrate while its dependence is sinusoidal in the film, as expected for the behavior of a confined mode.

### 5.2.1 Waveguide Structures

Undoubtedly, the optical fiber is the most ubiquitous optical waveguide structure. Integrated waveguides differ from optical fibers in that the integrated waveguide is fabricated on a planar structure using lithographic techniques. The planar geometry offers good control over the waveguide dimensions but suffers from higher attenuation. One of the simplest waveguide geometries is a channel waveguide, which consists of a rectangular core region surrounded on all sides by a cladding region. Other commonly used variants include ridge waveguide and rib waveguide.

There are many candidate materials for building integrated optical waveguides, including compound semiconductor materials (InP, GaAs), glass materials (SiO<sub>2</sub>, GeO<sub>2</sub>), polymers and other single-crystal dielectric materials (LiNbO<sub>3</sub>). Each of these materials has advantages and disadvantages in terms of the intrinsic material loss, cost, ease of fabrication, availability of deposition and growth technologies, and integrability. Lithium niobate is an attractive single crystal material for fabrication of optical waveguides because of its acousto-optic and electro-optic properties [55]. For the general overview of material properties of LiNbO<sub>3</sub>, the reader is referred to the Appendix. Single crystal LiNbO<sub>3</sub> has the property that mechanical stress in the material can change the optical index of refraction, and likewise an applied electric field can induce a change in index. Due to these properties of active modulation of the refractive index, LiNbO<sub>3</sub> is an attractive waveguide material for applications such as optical modulators [56], switches [57], sensors [58] and filters [59] etc.

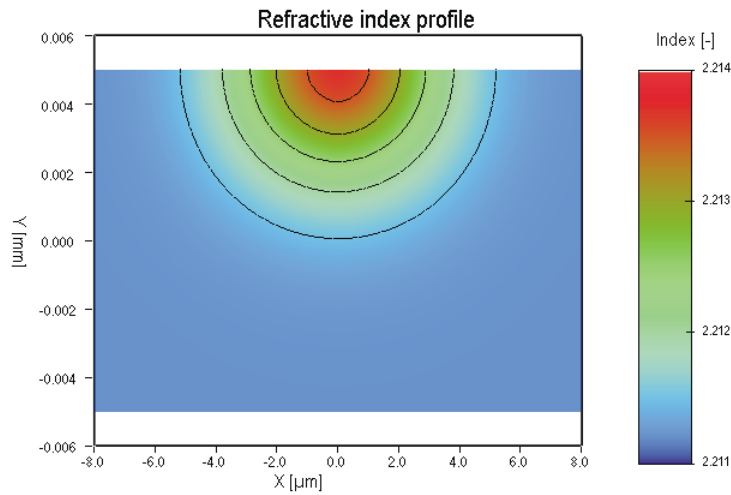


Figure 5.2: Simulated refractive index profile of a Ti-indiffused waveguide in  $\text{LiNbO}_3$ .

However, forming a waveguide structure in crystalline  $\text{LiNbO}_3$  is not as straightforward as for semiconductor materials or for doped glasses. Usually, the core region of the channel waveguide is formed by proton-exchange or metal diffusion [52, 55, 60]. These methods typically yield a graded-index channel waveguide profile as shown in Fig. 5.2.

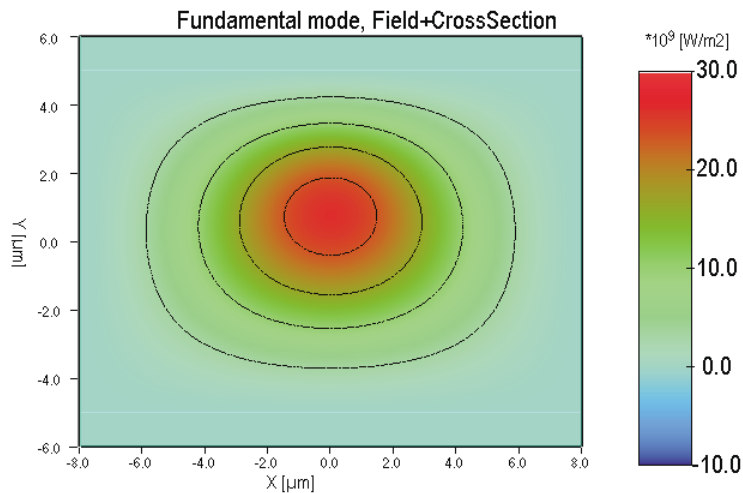


Figure 5.3: Fundamental mode of a Ti-indiffused channel waveguide in  $\text{LiNbO}_3$ , simulated using the effective index method.

In channel waveguides, the light is confined in two directions, allowing the propagation in only one direction and thus the radiation can propagate without suffering diffraction, that will otherwise give rise to power loss. Therefore, a channel waveguide is the right choice for applications like modulation, switching, filtering, amplification etc. in optical

networks. There are no pure TE or TM modes in channel waveguides, but instead there are two families of hybrid transversal electromagnetic modes (TEM), which depending on the alignment of the major component of the electric field are known as quasi-TE and quasi-TM modes. An exact treatment of the modal characterization in 2D waveguides is difficult and thus, there are number of numerical methods such as Marcatili's method and the effective index method [54] used for modal calculations. Fig. 5.3 shows the fundamental mode of the Ti-indiffused channel waveguide in LiNbO<sub>3</sub> simulated using the effective index method.

Channel waveguides fabricated in LiNbO<sub>3</sub> via well-established titanium in-diffusion exhibit very low losses and are used for most of the above stated applications. Iron-doped Ti-indiffused channel waveguide for single-mode operation at 1550 nm wavelength were used during this work for the realization of waveguide gratings. Fig. 5.4 shows the surface topography of such a waveguide using SEM (Scanning Electron Microscopy) and AFM (Atomic Force Microscopy) tools.

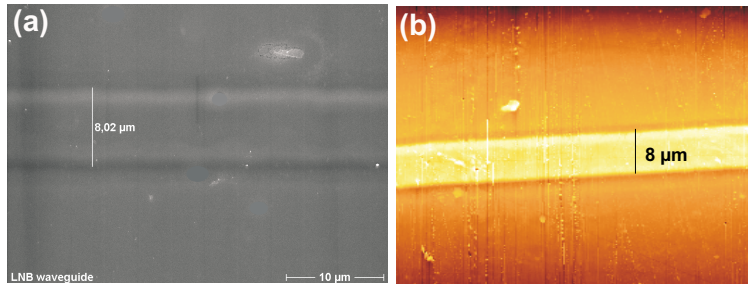


Figure 5.4: Surface topography of a Ti-indiffused channel waveguide in LiNbO<sub>3</sub>: (a) SEM image and (b) AFM image.

## 5.2.2 Waveguide Couplers

Considering the micron sized dimensions of the waveguides, coupling optical energy into or out of a waveguide is a very critical issue. The methods that are employed for coupling an optical beam between two waveguides (e.g. an optical fiber and a channel waveguide) are different from those used for coupling an optical beam in free space to a waveguide. Various types of couplers and coupling techniques are available for coupling efficiently to a particular mode (for the case of a multimode waveguide) with good efficiency. Coupling efficiency is usually defined as the fraction of total power in the optical beam, which is coupled into or out of the waveguide. Coupling efficiency depends most strongly on the degree of matching between the field of the optical beam and that of the waveguide mode.

Transverse coupling of laser beam to a waveguide is the simplest method. The beam is directly focused onto an exposed cross-section of the waveguide using a lens and this technique is known as direct focusing or end-fire approach. Transverse coupling between two

solid waveguides is done using end-butt coupling where polished or cleaved cross-sectional faces are butted together. However, transverse coupling is not useful when it is necessary to couple light into a waveguide that is buried within an optical integrated circuit, with only the top surface exposed. In this case, light is focused at an oblique angle onto the waveguide surface using a prism coupler [61]. Prism coupler is, however, not useful in practical applications because of vibration and temperature variations encountered. Gratings are very efficient for coupling light via phase-matching between a particular waveguide mode and an unguided optical beam which is incident at an oblique angle to the surface of the waveguide. Grating couplers [62] are widely used due to simple realization, reproducibility and compatibility with the planar device technology.

With the development in optical communication systems, efficient coupling of an optical beam from a fiber (used for long distance transmission) to a waveguide (e.g. used for signal processing) or vice-versa is often required. This task is challenging due to the intrinsic differences in the geometry of circularly symmetric fiber cores and nominally square-core planar waveguides [63]. The connection of optical fibers to waveguides can be achieved using a number of existing techniques such as alignment and gluing of cores [64], fusion technology or recently developed self-aligning pigtailling [65]. Most of the above-mentioned techniques are used for making permanent connections with precise alignment. However, for laboratory testing or waveguide characterization, end-butt coupling is generally used. The cleaved end of the fiber is directly butted in contact with the waveguide in an end-on alignment. An index-matching fluid is used to reduce reflection losses at the interface. For very small waveguide dimensions and for better alignment between the fiber-end and the waveguide-end, piezoelectrically driven micromanipulators are used.

During this work, Ti-indiffused channel waveguides with a cross-section  $8 \mu\text{m} \times 3 \mu\text{m}$  were used. Initial aim was to efficiently couple a light beam from a laser via a single-mode optical fiber patch cable into the waveguide. For this purpose, the fiber-end was cleaved using an ultrasonic cleaver. The cleaved fiber-end was then placed in a v-groove and installed on a mechanical xyz stage for alignment. The cleaved fiber-end was then aligned (with the help of a microscope) with the waveguide cross-section and butted in contact with the waveguide with a drop of the index-matching fluid at the interface. The single-mode fiber has a core size between  $8\text{-}10 \mu\text{m}$ . Due to the mismatch of size and geometry between the fiber and the waveguide, the light from standard cleaved fiber could not be efficiently coupled into the waveguide. We then tested a fiber with a lens at one end (lensed fiber) as shown in Fig. 5.5(a). Such lensed fibers are commercially available. A lensed fiber with  $15 \mu\text{m}$  focal length and  $7 \mu\text{m}$  spot size was used for coupling which could be easily done with higher coupling efficiency ( $\approx 60\%$ ). Fig. 5.5(b) shows a laser beam from a He-Ne laser at  $633 \text{ nm}$  being coupled to the channel waveguide from the lensed fiber (as viewed under the microscope).

The channel waveguides used during this work are designed for single-mode operation at telecommunication wavelength  $1550 \text{ nm}$  in the infrared (IR) range. The aim was to realize a Bragg grating in the waveguide and to demonstrate a spectral filter for optical

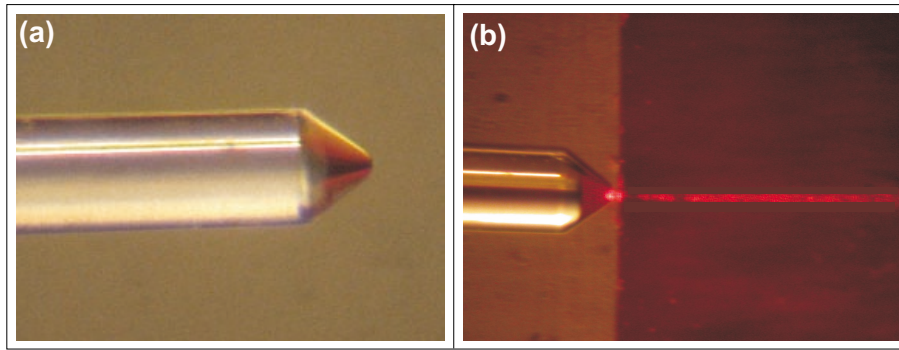


Figure 5.5: (a) Tip of the lensed fiber and (b) coupling of laser beam via the lensed fiber into the waveguide.

telecommunications. Before coupling the invisible IR wavelength, for the ease of adjustment and in order to locate the position of the waveguide, visible wavelengths from a Nd:YAG laser (@ 532 nm) or a He-Ne laser (@ 633 nm) were coupled. After coupling visible wavelengths, the other end of the fiber cable was switched to the IR laser and with little adjustments, the IR wavelength was coupled into the waveguide. Fig. 5.6 shows the CCD camera pictures of the output-edge of the waveguide via a lens. The fundamental mode of the waveguide as shown in Fig. 5.6(a) was excited at 1550 nm. At 532 nm, a higher order mode of the waveguide was excited as shown in Fig. 5.6(b). As the waveguide was designed for single-mode operation at 1550 nm, higher order modes are excited at shorter wavelengths. In order to verify that the Fig. 5.6(a) shows the fundamental mode, the far-field intensity pattern of the mode captured on a CCD camera screen (Fig. 5.7(a)) was calculated along the horizontal and vertical cross-sections. These calculated far-field intensity patterns were compared with the simulated ones (as shown in Fig. 5.7(b) & (c)) showing a good match and thus verifying that the coupled light is the excited fundamental mode.

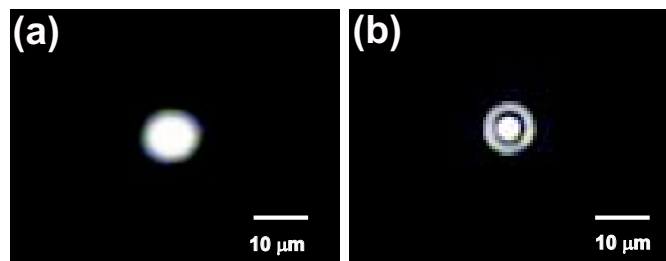


Figure 5.6: Coupled mode of the waveguide: (a) fundamental mode excited at 1550 nm and (b) higher order mode excited at 532 nm

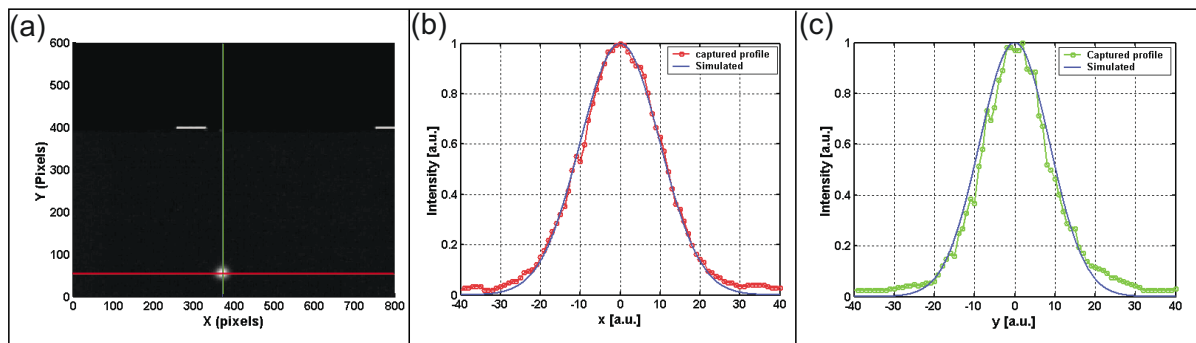


Figure 5.7: Verification of the coupled mode of the waveguide: (a) coupled mode captured at the CCD camera (800x600 pixels), (b) comparison of the horizontal cross-section of the captured far-field intensity pattern with a simulated pattern, and (c) comparison of the vertical cross-section of the captured far-field intensity pattern with simulated pattern

### 5.3 Waveguide Gratings

Waveguide gratings [66] are periodic perturbations induced in planar or channel waveguides, and are widely used in integrated photonics technology to perform a variety of functions such as input/output coupler, modal converter, reflector etc. The main task of a grating integrated in a waveguide structure is to allow coupling between modes that otherwise would remain independent. Under specific conditions, this characteristic allows the power transfer between collinear modes of different order, between counterpropagating modes and also between guided and radiation modes. Waveguide gratings have a great range of applications because of their intrinsic selectivity in terms of wavelength, modal propagation constant of the modes or angle in the case of radiation modes. Some of the well-known applications of waveguide gratings include feedback reflector for integrated lasers [67], in- and out-couplers [68], integrated sensors [69] and wavelength filters as described during this work. Two types of waveguide gratings will be discussed and described in the next sections. The first kind of waveguide gratings is the index modulation type grating as shown in Fig. 5.8(c). An index modulation grating can be formed by various techniques, e.g. by titanium-implantation [70] or by proton-exchange [71] in Ti:LiNbO<sub>3</sub> waveguides or by high contrast polymer filling in polymer waveguides [72]. Here, we realized index modulation gratings in Ti:LiNbO<sub>3</sub> channel waveguide via the photorefractive effect as discussed in chapter 3. The second kind of waveguide gratings is relief or corrugated grating as shown in Fig. 5.8(b), realized using photolithographic techniques.

Before proceeding to the realization and characterization of waveguide gratings, it is important to consider the basic theory of coupling between modes of the waveguide via the grating integrated in the waveguide. Some illustrious references dealing with the topic of coupled mode theory of waveguide gratings include [73–76]. However, for the concise introduction to the theory of waveguide grating, I would follow the approach discussed

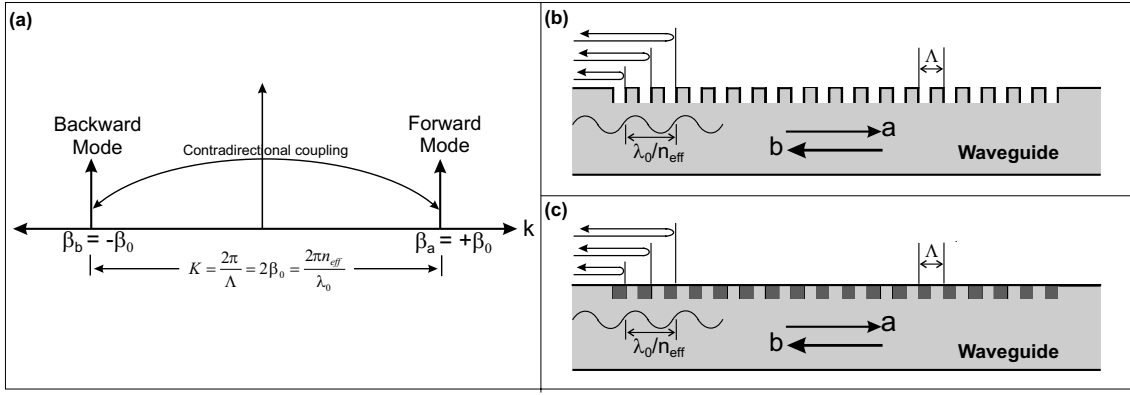


Figure 5.8: Contradirectional coupling via a grating in the waveguide: (a)  $k$ -space representation of coupling (phase-matching) between counterpropagating modes of the waveguide in the presence of a grating, (b) a corrugated grating in the waveguide showing coupling in real space which is termed as reflection from subsequent teeth leading to constructive interference, and (c) an index modulation grating in the waveguide depicting the principle of reflection

by G. Lifante in [54]. The theory is valid for both types of gratings mentioned above as they can be described by the spatial change in the dielectric permittivity  $\Delta\varepsilon$ . As  $\Delta\varepsilon$  is a periodic function, it can be mathematically expressed as a Fourier expansion of the form

$$\Delta\varepsilon(x, z) = \sum \Delta\varepsilon_q(x)e^{[-iqKz]} \quad (5.12)$$

where  $\mathbf{K}$  is the grating wavevector related to the grating period  $\Lambda$  as

$$|\mathbf{K}| = K = 2\pi/\Lambda \quad (5.13)$$

If a wave with a wavevector  $k$  ( $= 2\pi/\lambda$ ) is incident in the grating region, as a result of the periodic phase modulation  $\Delta\varepsilon$  induced by the periodic perturbation, several diffracted waves are generated, having wavevectors  $k + q\mathbf{K}$ ,  $q$  being an integer number. For the coupling between two guided modes induced by the grating, propagation constants of the modes  $\beta_a$  and  $\beta_b$  must fulfill the following relation

$$\beta_b = \beta_a + qK \quad (5.14)$$

where  $q$  indicates the coupling order. This relation is called the Bragg condition or the phase matching condition for the guided modes in waveguides. Coupling can occur between two codirectional modes or between the counter propagating (contradirectional) modes. As we are going to discuss reflection filters based on waveguide gratings, only the case of contradirectional coupling will be described here. In this case, the coupling takes place between two collinear modes  $a$  and  $b$  that propagate in opposite directions, if the propagation constants of the modes have opposite signs (e.g.  $\beta_a > 0$  and  $\beta_b < 0$ ). For the case of single-mode waveguides,  $a$  and  $b$  are the same mode in the same waveguide,

but with opposite propagation directions. For the case when the propagation constants of the guided modes  $\beta_a$  and  $\beta_b$  fulfill the phase matching condition for the  $q^{th}$  coupling order ( $\beta_b = \beta_a + qK$ ), and no other combination of modes fulfills that relation, the modal coupling equations are written as:

$$\pm \frac{dA(z)}{dz} = -i\kappa B(z)e^{-i2\Delta z} \quad (5.15)$$

$$\pm \frac{dB(z)}{dz} = -i\kappa A(z)e^{+i2\Delta z} \quad (5.16)$$

where  $A(z)$  and  $B(z)$  are the modal amplitude coefficients for the forward propagating mode a and the backward propagating b, respectively,  $\kappa$  is the coupling coefficient and the mismatch parameter  $2\Delta$  is defined as:

$$2\Delta = \beta_b - (\beta_a + qK) \quad (5.17)$$

and denotes the deviation with respect to the perfect phase matching condition, taking into account the effect of periodic structure via  $q^{th}$  order coupling. In order to calculate the modal amplitude coefficients and hence the coupling efficiency, equations (5.15) and (5.16) are solved in the case of light injection at  $z = 0$  by exciting selectively the mode a and for the grating length  $L$ . Taking into account the initial boundary conditions  $A(0) = 1$  and  $B(L) = 0$ , the solutions of coupled mode equations (5.15) and (5.16) for a situation near the phase matching condition, are

$$A(z) = e^{-i\Delta z} \frac{\alpha \cosh[\alpha(z-L)] + i\Delta \sinh[\alpha(z-L)]}{\alpha \cosh(\alpha L) - i\Delta \sinh(\alpha L)} \quad (5.18)$$

$$B(z) = e^{+i\Delta z} \frac{i\kappa \sinh[\alpha(z-L)]}{\alpha \cosh(\alpha L) - i\Delta \sinh(\alpha L)} \quad (5.19)$$

where the parameter  $\alpha$  is defined by  $\alpha \equiv (|\kappa|^2 - \Delta^2)^{1/2}$ . For the present case of contradi-rectional coupling, the coupling efficiency, defined as the quotient of the power associated with the mode b at position  $z = 0$  with respect to the mode a at the same position, yields:

$$\eta = \frac{|B(0)|^2}{|A(0)|^2} = \left[ \frac{\sinh^2 \alpha L}{\cosh^2 \alpha L - \Delta^2 / |\kappa|^2} \right] \quad (5.20)$$

For a given grating length, the efficiency is maximum at the phase matching condition ( $\Delta = 0$ ) as given by

$$\eta = \frac{|B(0)|^2}{|A(0)|^2} = \tanh^2(|\kappa|L) \quad (5.21)$$

From the above equation, for a grating with length  $L = \pi / |\kappa|$  in the waveguide, the efficiency is near 0.99, indicating a near total power transfer between the counterpropagating

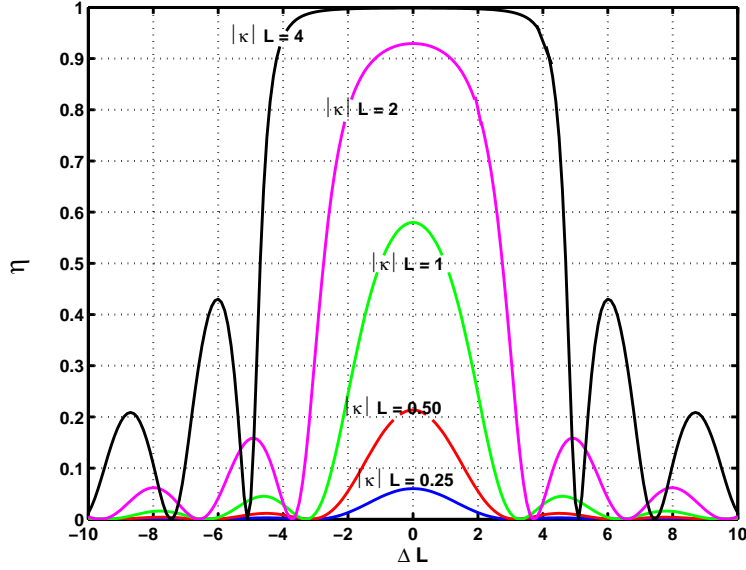


Figure 5.9: Coupling efficiency or the reflection spectra of the grating for five different  $|\kappa|L$  values plotted against the normalized deviation from the phase matching or Bragg condition.

modes. So far, we have discussed the situation in  $k$ -space as illustrated in Fig. 5.8(a) i.e. in terms of propagation vectors. Another way of analyzing the problem in real space is to consider the waveguide grating as periodic perturbation in the waveguide that reflects a portion of the incident light into the counterpropagating mode [77]. As with other forms of Bragg reflection, in order for the reflected light to constructively interfere, the path difference between the reflected light from subsequent grating periods must be an integral multiple of wavelengths. For the strongest reflection to occur, the path difference must be precisely one wavelength, meaning the grating period must be one half of the wavelength (Bragg condition):

$$\Lambda = \frac{\lambda_0}{2n_{eff}}. \quad (5.22)$$

Here,  $\Lambda$  is the grating period,  $\lambda_0/n_{eff}$  is the wavelength of light inside the dielectric material, and  $n_{eff}$  is the effective index of refraction inside the guiding dielectric structure. The principle of reflection from a Bragg grating in the waveguide is illustrated in Fig. 5.8 (b) and (c). So the coupling efficiency in eqn. (5.20) is the reflection coefficient of the grating as well, considering the problem in real space. Power transfer between the counterpropagating modes or the reflection coefficient of the grating mainly depends on the length of the grating and on the coupling coefficient  $\kappa$ , which in turn depends on the grating strength (index modulation in case of photorefractive gratings and grating depth in case of relief gratings). Fig 5.9 shows the coupling efficiency or the reflection coefficient for five different  $|\kappa|L$  values as a function of normalized deviation ( $\Delta L$ ) from the phase matching or Bragg condition. Apart from the length and the grating strength, there are many other parameters such as profile and alignment of the grating in the waveguide, which have to

be precisely optimized in order to get the desired functioning of the waveguide gratings as discussed in [78].

### 5.3.1 Photorefractive Reflection Gratings

As discussed in the previous section, waveguide gratings allow efficient coupling between counterpropagating modes and hence can be used as wavelength selective filters. In this section, the realization of photorefractive gratings in the waveguide for the application as reflection filters for telecommunication wavelengths will be discussed. In addition, the tuning of the filtered or reflected wavelength via electrical control will be described.

#### Design and Realization

The theory of the photorefractive effect was discussed in detail in chapter 3. The photorefractive gratings were realized in bulk LiNbO<sub>3</sub> crystals for the realization of holographic lenses and mirrors as discussed in Chapter 4. Photorefractive gratings exhibit high wavelength selectivity and narrow bandwidth and therefore are widely used as wavelength filters. Fig. 5.10. shows the plot of diffraction efficiency as a function of grating length and fractional wavelength detuning for a photorefractive reflection grating with period of 350 nm, grating strength (index modulation)  $\delta n = 10^{-4}$  and Bragg wavelength  $\lambda_B = 1550$  nm. It can be seen that even for small index modulation, almost 100% diffraction is possible for relatively longer gratings. Bulk implementation of the the photorefractive grating based filters has been discussed in [79–82]. However, integrated implementation of such filters is promising for optical communication systems, e.g. DWDM, optical sensors, narrow bandwidth integrated waveguide lasers etc. and has been discussed alongwith the thermal fixing of photorefractive gratings in [83–86].

For the realization of an electrically tunable integrated optical filter, the photorefractive gratings were realized in a LiNbO<sub>3</sub> channel waveguide, doped with iron and copper in order to increase the photorefractive sensitivity. The photorefractive gratings were recorded in transmission geometry, while the readout was done in reflection geometry. This means that the recording wavelength differs from the diffracting wavelength. This principle is well known and was efficiently used in [87–89], where a recorded holographic grating was thermally fixed in LiNbO<sub>3</sub>. In our case, we did not use any fixing techniques in order to make the gratings permanent for two reasons: firstly, it gave the possibility to easily erase and record a new grating, which is very convenient for the experimental purposes and we did not need to use complicated fixing techniques to make gratings permanent, and secondly, LiNbO<sub>3</sub> has very low dark conductivity and it can hold the grating for few days upto few months depending upon the crystal quality. The non-fixed grating could be stored for several days without noticeable degradation. However, in commercial devices, the gratings should be fixed by the technique of thermal fixing, which gives excellent results.

The grating was recorded by the interference of two coherent plane waves of an argon-ion laser at  $\lambda_W = 458$  nm (Fig. 5.11(a)). The two coherent beams with  $\theta = 40.7^\circ$  impinge

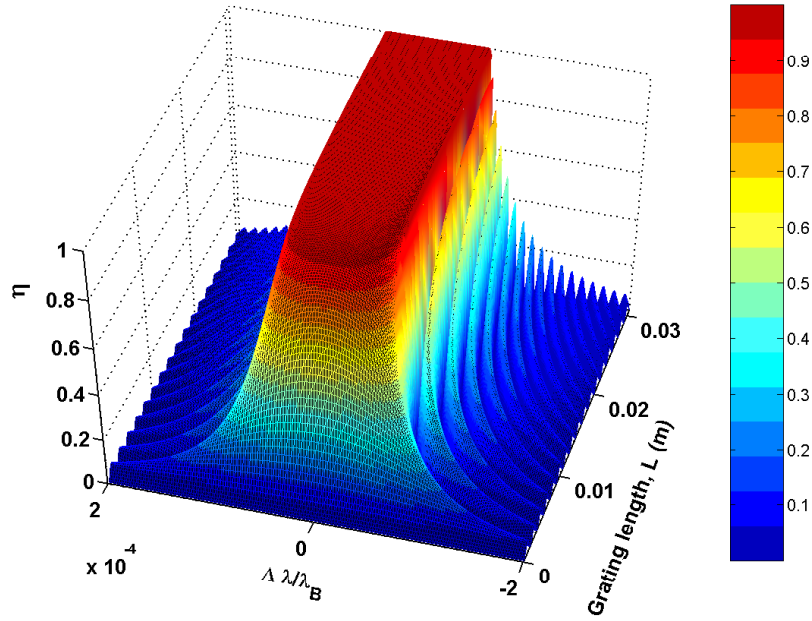


Figure 5.10: Plot of diffraction efficiency  $\eta$  vs. grating length  $L$  and fractional wavelength detuning  $\Delta\lambda/\lambda_B$  for  $\lambda_B = 1550 \text{ nm}$ ,  $\Lambda = 350 \text{ nm}$ , and  $\delta n = 10^{-4}$ .

upon the waveguide and illuminate the top face of the crystal with the waveguide. The wavevector  $K$  of the generated standing-wave interference pattern was directed along the waveguide channel and the grating with a period of  $\Lambda \approx 351 \text{ nm}$  was recorded. The typical recording time in order to have more than 90% diffraction efficiency was approximately 1.5

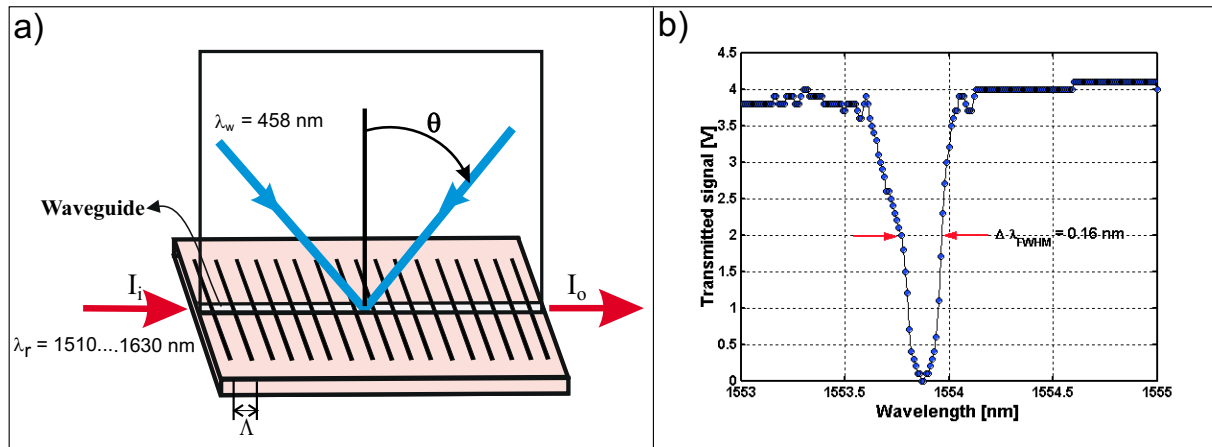


Figure 5.11: Holographic recording of photorefractive gratings. a) Recording with blue wavelength ( $\lambda_w = 458 \text{ nm}$ ) and read-out with infra-red wavelength ( $\lambda_r \approx 1550 \text{ nm}$ ), and b) Transmission spectrum of an 8 mm long grating.

hours for the used crystals. The whole set-up was mounted on a vibration isolated optical table in order to reduce the effect of external vibrations. In addition, the whole set-up was covered with a metallic chamber with just one small inlet for the laser beam, in order to reduce perturbations due to air turbulence. These measures helped in recording good quality gratings with high diffraction efficiency. However, for practical applications and commercial devices, active stabilization techniques [90,91] should be used for recording in order to compensate for environmental phase perturbations leading to degradation of the grating.

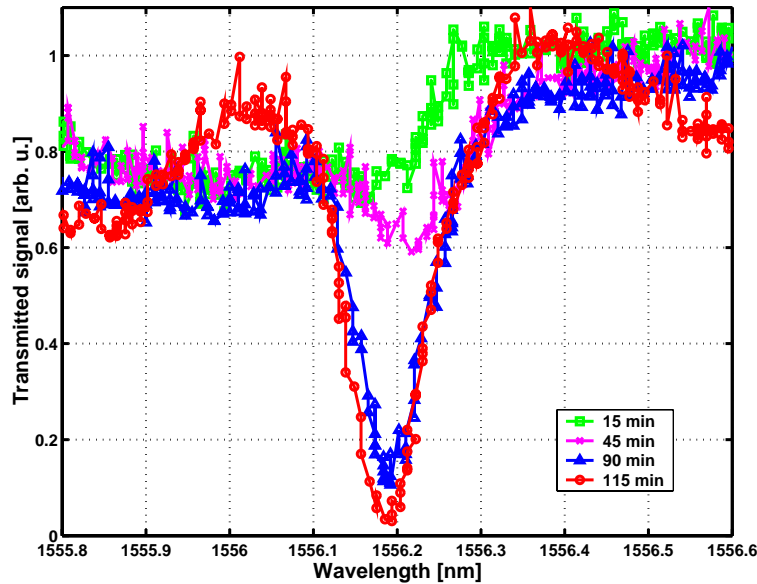


Figure 5.12: Temporal build-up of the photorefractive grating.

### Measurements with the Realized Grating Filter

For the read-out, single mode optical fiber pigtails were attached at both ends of the waveguide and light from a tunable laser was coupled via one of these fibers. The other end was attached to the photodetector in order to record the transmission spectrum by measuring the optical power at the output end as a function of the read-out wavelength. Fig. 5.11(b) shows the transmission spectrum of an 8 mm long recorded grating with almost 100% diffraction efficiency. The bandwidth of the grating is about 0.16 nm and the central reflection wavelength is 1553.9 nm which makes such waveguide grating filter useful for DWDM telecommunication devices. Though the result is shown for one central wavelength, the range of operation of the filter could be extended to complete C- and L- optical communication bands by changing the angle between the beams recording the grating. It was also interesting to monitor the process of build-up of the grating (as shown in Fig. 5.12) over time as read-out was done simultaneously with the recording. One

important thing to note here is that read-out light did not destroy the recording as lithium niobate is not sensitive for IR wavelengths, which were used for simultaneous read-out.

The measured spectral transfer function of the grating was closely studied. Kogelnik's theory as discussed in section 2.3.2 in chapter 2 was used for the simulation and for the fitting to the experimentally measured data. Fig. 5.13 shows that the spectral transfer function measured for the 8 mm long grating fits nicely except the sidelobes to the simulated transfer function for the 7.8 mm grating with a period of 351.32 nm. The solid line represents the simulated result and the circles represent the measured data. The parameters used for fitting are mentioned in the plot. The absence of side lobes in the measured data can be attributed to an apodized grating i.e the amplitude of the grating is not constant over the whole length of the grating. Another reason for the missing side-lobes can be absorption. However, the absorption was negligible when measured. Basically, the gaussian profile of the laser beam usually leads to an apodized grating. Kogelnik's theory, however, considers only non-apodized gratings and so, the side lobes are present in the simulated plot.

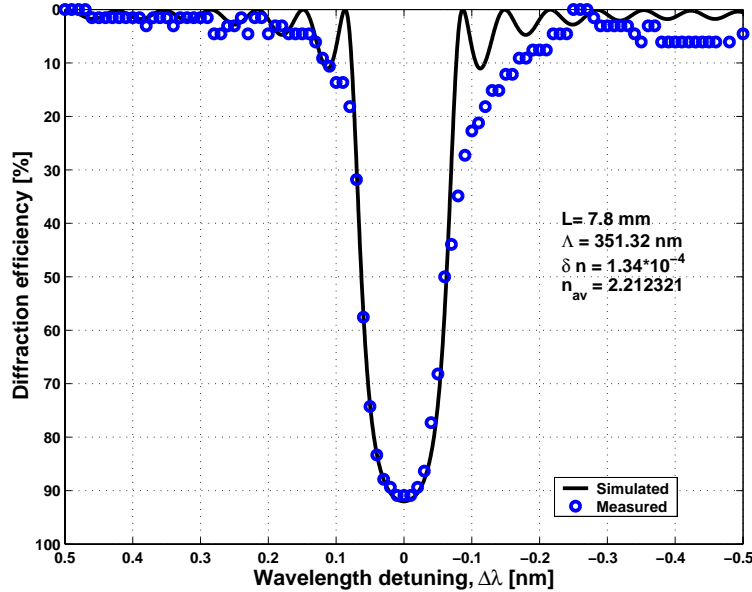


Figure 5.13: Spectral transfer function of the grating: simulated and measured data.

After the realization of a photorefractive grating in the waveguide with quiet high diffraction efficiency, in the next step, the diffraction was electrically tuned. Since the grating was recorded in electro-optical lithium niobate, the effective index of the waveguide  $n_{eff}$ , and hence the central wavelength  $\lambda_B$  can be controlled by an external electric field. The principle of electrical control was discussed in detail in chapter 4. The tuning of the spectral transfer function without a change in shape takes place when the applied field is homogeneous along the grating. The application of an inhomogeneous field will modify

the spectrum of the reflected (diffracted) light. By setting a certain spatial distribution of the applied electric field along the grating, it is possible to obtain a spectral transfer function of a desired shape. In other words, the transfer function can be synthesized as will be discussed in the next chapter.

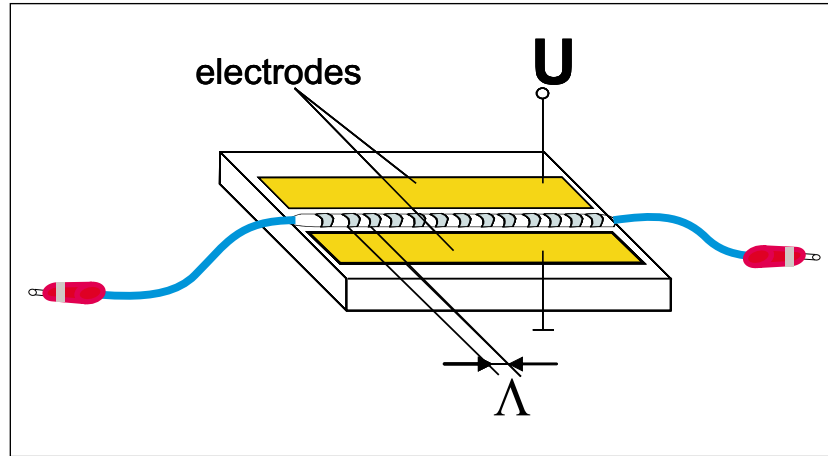


Figure 5.14: Sketch of the photorefractive grating filter with electrodes deposited for electrical tuning of the spectral transfer function of the filter.

The electrical control was provided by means of copper electrodes deposited onto the substrate surface on both sides of the waveguide as shown in Fig. 5.14. The spacing between the electrodes was  $d = 20\mu\text{m}$ . For thin planar film electrodes [92], the electric field strength in the waveguide was  $E = 2U/\pi d$ , where  $U$  is the voltage applied to the control electrodes. The waveguide surface was covered with a silica film in order to protect the waveguide from dust and moisture. This structure made it possible to obtain a sufficiently homogeneous electric field in the waveguide region. The crystal was then packed in a protective coverage.

Once the grating with more than 90% diffraction efficiency was recorded, a dc voltage was applied to the electrodes in order to change the effective index in the waveguide region which in turn leads to a change in the central reflected (diffracted) wavelength. Continuous tuning of the dc voltages leads to a continuous change in the effective refractive index and hence leads to a continuous tuning of the filtered wavelength. The spectral transfer function of the filter was measured before and after the application of the control voltage. As discussed in chapter 4, positive and negative polarity of the applied voltage leads to a decrease or an increase in the refractive index (via electro-optic effect) depending upon the orientation of the crystal and the polarization of the incident light. Therefore, both the polarities of the applied dc voltage can be used to tune the filtered wavelength in opposite directions as shown in Fig. 5.15. The spectral response of the grating filter is shown for three different values of the applied electric field as mentioned in the figure. With increasing value of the applied field, the spectral transfer function could be continuously tuned. With an applied

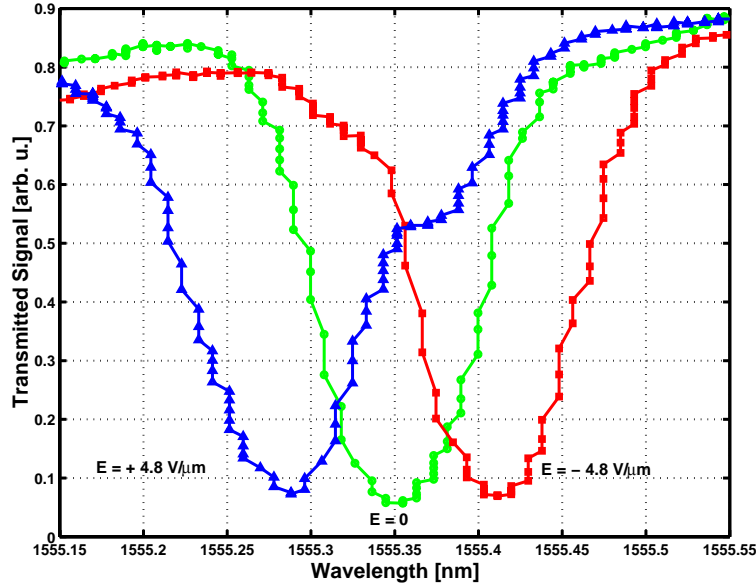


Figure 5.15: Experimental demonstration of continuous tuning of the central wavelength of the integrated optical filter for three different values of the applied external field.

electric field between  $\pm 4.8 \text{ V}/\mu\text{m}$ , the total continuous tuning range was 0.14 nm. Though the total tuning range is limited, the range of operation of the filter could be extended to C- and L-bands by changing the parameters of the recording. The reversible photorefractive materials offer the advantage of multiple erasure and recording provided the grating was not fixed. The steps observed in the measured data are due to the tunable IR laser as it did not have continuous tuning facility and had to be tuned in steps using a Labview program. It can be seen that the width of spectrum (reflection bandwidth) is about 0.1 nm and the spectral shift of the peak of the transfer function for the applied field of  $4.8 \text{ V}/\mu\text{m}$  is 0.07 nm. These values are in satisfactory agreement with the theory. Shift of the central wavelength is calculated via the electro-optic effect as:

$$\delta\lambda_B = \frac{n^2 r_{eff} \lambda_B E}{2} \quad (5.23)$$

where  $\lambda_B$  is the filtered or reflected wavelength,  $n$  is the effective refractive index,  $r_{eff}$  is the effective electro-optic coefficient and  $E$  is the externally applied electric field. The shift in the central wavelength reported here is not the maximum and can be increased with application of higher voltages. The continuous tuning of the spectral transfer function is, however limited by the breakdown voltage as discussed in chapter 4 also. By further optimization of the crystal and waveguide orientation and electrode configuration, it is possible to improve the working parameters considerably. The results presented in this section verify the implementation of the electrical control of diffraction from photorefractive gratings and demonstrate the principle of real-time electrical tuning of the spectral transfer function.

### 5.3.2 Photolithographic Gratings

This section is concerned with the design and fabrication of surface-relief gratings in lithium niobate waveguides. The fabrication sequence is described in detail and results on electrical control of corrugated lithium niobate waveguides are presented at the end of this section.

At this point, it is important to consider the need for moving on from photorefractive gratings to surface-relief gratings. When considered for practical applications and commercial devices, the photorefractive grating poses certain disadvantages. The limitations include the non-permanent nature of the photorefractive gratings and their sensitive fabrication process. Moreover, it is not possible to use mass-production techniques for such gratings. Photorefractive gratings are refractive index gratings formed by distribution of charges inside the material. These charges tend to settle over time and lead to the erasure of the grating. The lifetime of such a grating depends on the material properties such as dark conductivity. However, there are techniques like thermal fixing which are effectively used to make the gratings permanent. But, such techniques are complicated and expensive. In addition, the grating has to be individually recorded each time and preferably with an active stabilization technique. Relief gratings on other hand are permanent structures and can be fabricated easily with the existing standard photolithographic techniques involving deposition, holographic exposure, dry and wet etching. Moreover, once a good-quality master mask is prepared, mass-production techniques can be used to produce such gratings.

#### Design and Fabrication

Dielectric surface-relief (or corrugated) gratings are of considerable interest owing to their many applications in quantum electronics, integrated optics, spectroscopy etc. Example devices include distributed-feedback (DFB) lasers, distributed-Bragg-reflector (DBR) lasers, beam deflectors, waveguide couplers, spectral filters, wavelength multiplexers and demultiplexers, beam combiners and others. During this work, surface-relief gratings were designed and fabricated in Ti:LiNbO<sub>3</sub> waveguides for the application as electrically tunable integrated optical filters. The first step towards the design of such a filter was to choose an optimum profile and shape of the grating in order to allow efficient coupling (or reflection) to the backward propagating mode of the waveguide. For this purpose, I surveyed the literature of surface-relief gratings in detail. Diffraction characteristics of relief gratings using different numerical techniques and mathematical approaches are nicely presented in [93–97]. A rectangular grating profile is preferred due to high diffraction efficiency and ease of fabrication. In [98], a detailed calculation is presented in order to study the influence of the profile of the corrugated grating used as a coupling element (coupling to other modes) on the filter performance and it is concluded that the rectangular profile gratings have highest coupling strength. Based on this detailed survey, a rectangular profile was chosen for the design.

The next step towards the design was to determine the grating period in order to achieve the coupling or reflection at a desired wavelength. As the chosen material for the design

is Ti:LiNbO<sub>3</sub>, the grating will be used in reflection geometry and the desired wavelength of operation is near 1550 nm (telecommunication wavelengths), the grating period ( $\Lambda = 2n_{eff}\lambda_B$ ) should be near 350 nm. For such small grating period, standard laser lithography can not be used to write the grating as the resolution ( $\approx 1 \mu\text{m}$  or more) for most of the laser lithography systems is limited. Therefore, holographic lithography was used to pattern the gratings firstly in photoresist and thereafter the patterned grating was transferred to the waveguide via dry-etching techniques.

Other important factors to consider are the depth of the grating grooves and the effective length of the grating. The grating has to be long enough to efficiently couple (or reflect) the incident light to the backward propagating mode as discussed in section 5.3. From eqn. (5.21), for a near total coupling (or reflection) to the backward propagating mode, the length of the grating should be  $L = \pi/|\kappa|$ . The coupling coefficient  $|\kappa|$  for the case of a corrugated waveguide grating is expressed as [99]:

$$|\kappa| = \frac{\pi h n_w^2 - n_{eff}^2}{\lambda 2W_{eff}n_w} \quad (5.24)$$

where  $\lambda$  is the wavelength,  $h$  is the peak-to-peak perturbation (grating groove) height,  $W_{eff}$  is the effective waveguide height,  $n_w$  is the refractive index of the waveguide, and  $n_{eff}$  is the effective index of the unperturbed mode. For the chosen waveguide material and dimension, assuming the grating depth  $h$  to be approximately 200 nm, the required grating length for the case of complete reflection would be about 1 cm. To fabricate a 1cm long homogeneous (coherent) grating is quite challenging. By coherent, we mean a grating without phase jumps or errors. As discussed in Section 5.3, the operation of the Bragg grating is based on the constructive interference between the light reflected from the successive grating teeth and for the constructive interference to occur, the grating must be coherent over its entire length.

There are various techniques that can be used to pattern the corrugated gratings such as laser lithography, electron-beam (e-beam) lithography and holographic or interferometric lithography. In e-beam lithography system, a scanning electron beam defines the grating pattern on a suitable mask. The disadvantage of this system is that an e-beam, system cannot produce a pattern that is coherent over a large area [77]. The patterns produced by an e-beam system are subject to distortions caused by charging of the substrate, electromagnetic and acoustic interference, lens aberration, and stage motion. Some of these distortions are systematic and can be corrected but distortions associated with motion of the stage introduce random errors which result in phase errors destroying the coherence of the grating. The limitation of resolution with laser lithography is already discussed above. There are some direct writing techniques like UV-pulse ablation [100, 101]. Such techniques are complicated and the grating profile cannot be easily controlled. In [102], surface patterning of lithium niobate is done by combined UV laser and wet etching, which is insensitive to the crystallographic orientation of the wafer. However, gratings produced by this technique also suffer from uncontrolled phase errors and producing a long coherent grating is cumbersome.

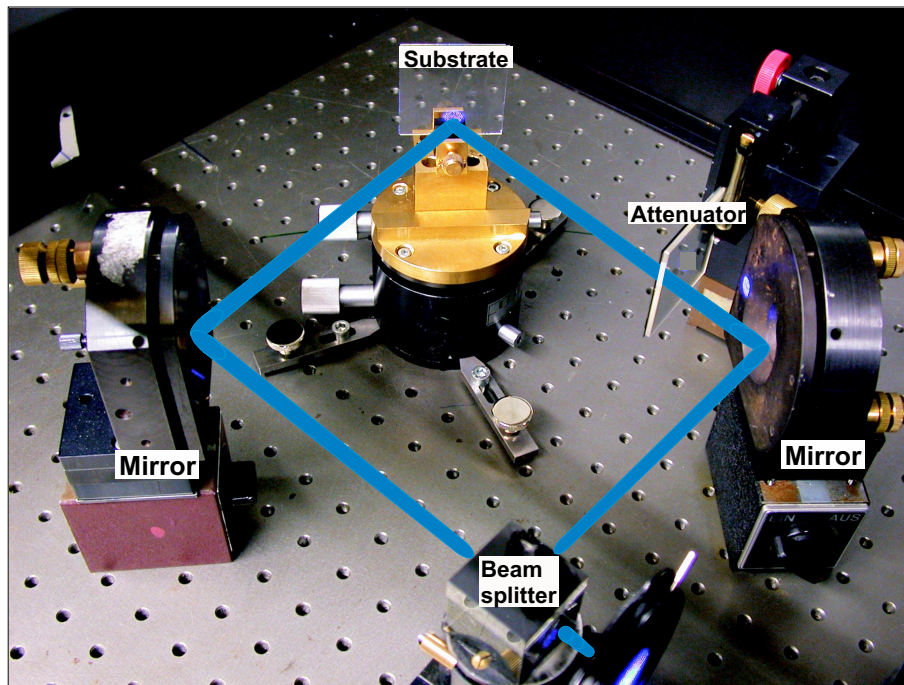


Figure 5.16: Holographic lithography set-up used for exposing the photoresist to the interference pattern.

Considering the design parameters and the literature survey, holographic or interferometric lithography was found to be the most suitable for the patterning of desired gratings in photoresist. Photoresist is a standard and most suitable material used for the patterning of integrated structures [103–105]. Nevertheless, it is difficult to achieve optimum results due to the number of parameters involved like exposure time, thickness and quality of resist films etc. involved in the fabrication. These problems have been addressed by a number of groups and one can find some illustrious solutions in [106–108].

Using the standard holographic lithography, a standing wave in space was formed by two coherent beams of an argon-ion laser at 458 nm interfering at an angle of  $\approx 81.5^\circ$  between the beams as shown in Fig. 5.16. The standing wave pattern was then used to expose a pattern in photoresist (standard Shipley S1805 positive photoresist), spin-coated on either on a substrate or a mask. A standard commercial phase mask can be used to directly expose the desired pattern in photoresist without making repetitive tests to optimize the working parameters. However, we prepared the mask ourselves and for this purpose, the gratings were initially realized in photoresist film on glass substrates in order to optimize the various recording parameters such as thickness of resist film, exposure time, development time etc. and to reach the desired grating design. Several sets of gratings were recorded with different parameters. The developed gratings were first tested for diffraction efficiency by placing them back in the interferometric set-up with one beam blocked. Some of the gratings with good efficiency from each set were further examined with scanning electron microscopy

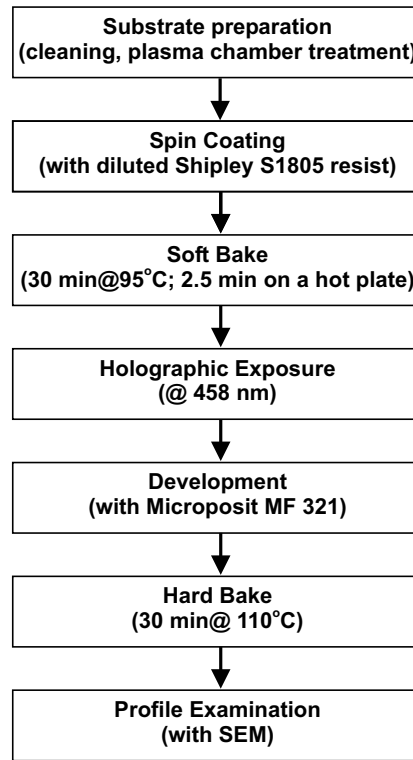


Figure 5.17: Process sequence for fabricating photoresist gratings.

(SEM) to check the profile, period and depth of the gratings. The general fabrication sequence is shown in Fig. 5.17 and Fig. 5.18 shows SEM pictures of some samples.

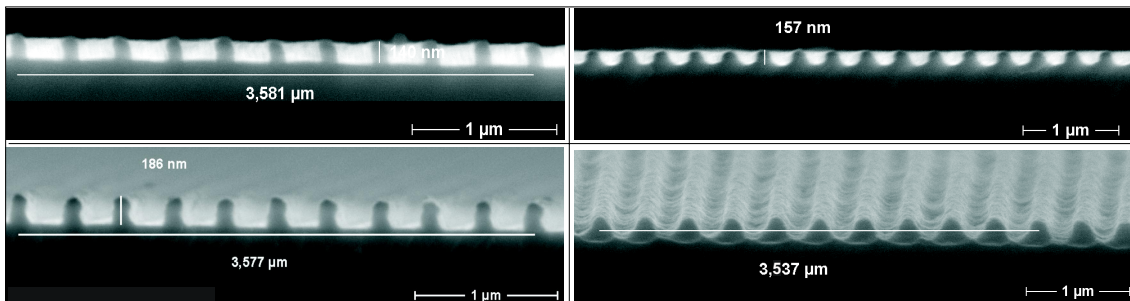


Figure 5.18: Scanning electron micrographs of photoresist grating on glass substrates.

After optimizing the working parameters, the photoresist was spin-coated directly on the crystal face with the waveguide. After following the standard process sequence as illustrated in Fig. 5.17, the waveguide surface was ready with the photoresist grating mask. The pattern has to be transferred from the mask to the waveguide surface. This is usually

done with ion milling [109, 110] or reactive ion etching (RIE). These techniques are commonly used for semiconductor materials in integrated circuits and for lithium niobate in integrated optical devices [55]. The process of pattern transfer from the photoresist mask to lithium niobate via RIE using  $\text{CHF}_3$ ,  $\text{C}_2\text{F}_6$ ,  $\text{Ar}/\text{O}_2$  has been explained in [111–113]. RIE of lithium niobate using  $\text{SF}_6$  also has been done as in [114]. Although none of the references reviewed discussed standard ion etching, etching of lithium niobate was tried with Argon-ion beam. In spite of an exposure as long as 3 hours, no noticeable damage to the surface was observed. This is understandable as lithium niobate is a very hard

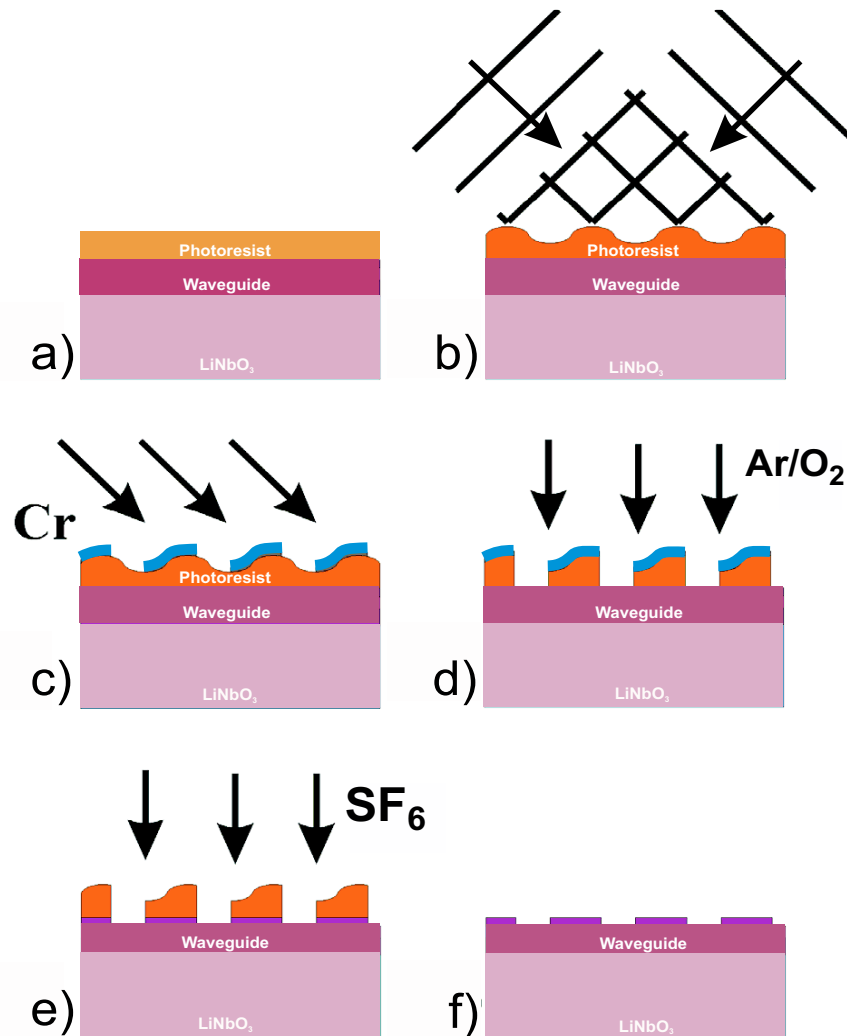
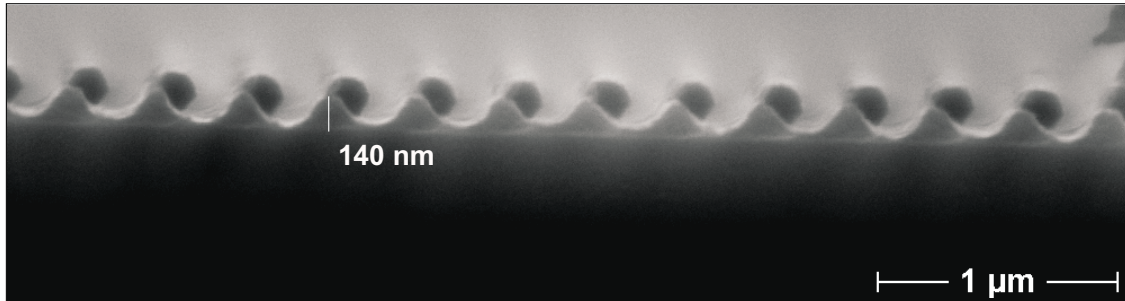


Figure 5.19: Sequence of technological processes to fabricate corrugated gratings in  $\text{LiNbO}_3$ . a) Deposition of photoresist via spin-coating; b) holographic lithography to expose the photoresist; c) shadowing with chromium as masking material; d)  $\text{Ar}/\text{O}_2$  ion etching to remove residual resist in grooves; e) reactive ion etching (RIE) with  $\text{SF}_6$ ; e) removal of residual chromium and resist

dielectric material (see Appendix). Another reason for this is not enough power in the ion beam achievable from the available machine. So, I decided to go ahead with reactive ion etching technique.

Before proceeding to the reactive ion etching of lithium niobate and the transfer of the grating pattern from the photoresist, a hard mask had to be prepared. Photoresist being a soft polymer material is easily stripped off by the ion beam. On the other hand a hard dielectric material like lithium niobate requires a strong ion beam for etching. Thus, a metal layer of chromium (Cr), Titanium (Ti) or Nickel (Ni) has to be evaporated onto the resist grating in such a way that the substrate (crystal surface) is still directly exposed to the ion beam for the etching. This is done by a technique known as shadow or slope evaporation [115] where the substrate is placed at a certain angle with respect to the source rather than placing it directly in line as done in usual evaporation techniques for thin film deposition. Depending on the relative etch rates of the lithium niobate and the metal used as hard mask for etching with a specific gas (e.g.  $\text{SF}_6$ ,  $\text{CHF}_3$  or  $\text{C}_2\text{F}_6$ ), the thickness of the metal film is chosen. Considering the literature reviewed,  $\text{SF}_6$  provides higher etching rate for lithium niobate as compared to other gases used and chromium is the most widely used hard mask. Using chromium as hard mask on the photoresist grating recorded on lithium niobate, RIE with  $\text{SF}_6$  was done in order to transfer the grating in the waveguide. Fig. 5.19 illustrates schematically the process sequence for fabricating the corrugated gratings in  $\text{LiNbO}_3$ .



*Figure 5.20: Scanning electron micrograph of a photoresist grating shadow evaporated with chromium.*

In order to obtain an optimized shape and thickness of the Cr mask, chromium was initially shadow evaporated at different angles on the photoresist grating on the glass substrates. These chromium masks were then examined with SEM as shown in Fig. 5.20. Finally, a 100 nm thick Cr layer was shadow evaporated onto the photoresist grating on lithium niobate at an angle of  $70^\circ$  with respect to the substrate normal. In the next step, the sample was exposed to Ar-ion etching which removes the residual photoresist (as seen in Fig. 5.20) in the grooves in order to provide the substrate directly available for ion attack. The power of the ion beam was not strong enough to harm the chromium layer which has to stay and serve as a hard mask for the following RIE. However, this step can also be done

with  $O_2$  plasma. Another way to do is to use photoresist solvents such as acetone or isopropanol or use liftoff techniques to completely remove the resist leaving just the chromium mask. We used different liquid solvents, but, everytime the grating was destroyed as it is a fine-period grating. After initial trials with liquid solvents, a mild ion beam etching proved much better results. This problem is also addressed in literature and an exposure to oxygen plasma has been suggested in order to get rid of the residual resist in grooves. In our case, a mild ion etching with Argon ions produced satisfying results.

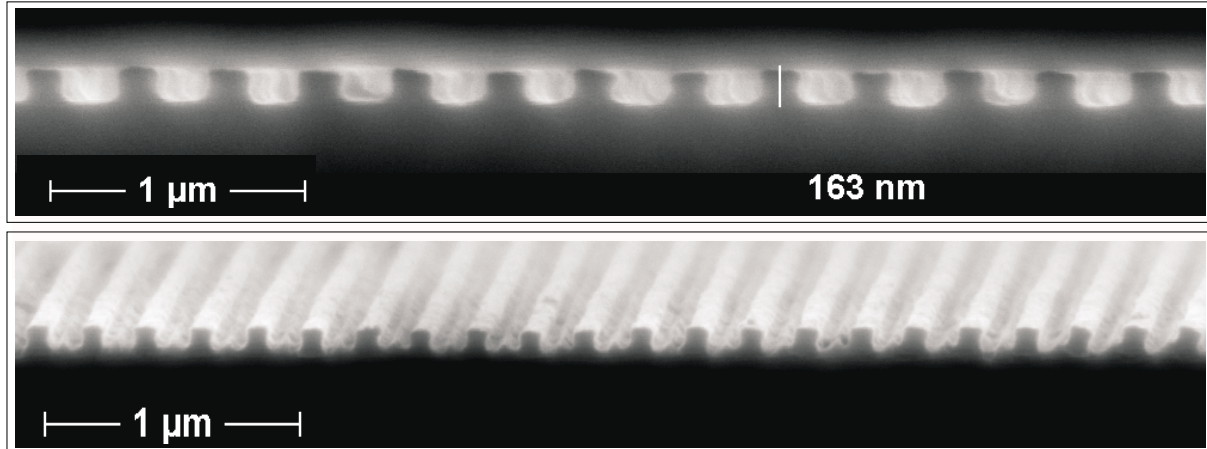


*Figure 5.21: Scanning electron micrographs of a chromium grating on glass substrate prepared after patterning a photoresist grating on chromium covered glass substrate followed by chromium wet etching.*

Apart from the procedure discussed for the preparation of the hard mask for RIE, another effective method was developed by us to get an optimum hard mask for etching. The substrate (glass or lithium niobate) was first sputtered with chromium in order to get an about 150 nm thick chromium layer. Photoresist was then spin-coated onto the chromium covered substrate. The standard steps of holographic exposure were followed by development and hard bake, leaving the chromium covered substrate with photoresist grating. However, the photoresist grating should have a 100% contrast for the following steps to be successful. The substrate was then wet-etched with chromium etchant ( $Ce(NH_4)_2(NO_3)_6 + CH_3COOH + H_2O$ ) which attacks only the exposed (no photoresist covered) chromium. The photoresist was later removed with acetone and iso-propanol. Following this procedure, a perfect rectangular chromium grating mask was achieved as shown in Fig. 5.21. The mask thickness could be varied by varying the initial thickness of the chromium film deposited. Although a good quality chromium mask was obtained with this method, it could not be further used due to the application for which the grating was fabricated. The grating is intended for electrical control via the electrodes deposited on the surface. In such case where high voltage has to be applied, the surface of the crystal should be clean enough not to provide any short circuit which can destroy the entire device. The chromium mask directly deposited over the crystal surface always leaves some metal

on the surface even after wet etching of chromium. The high temperature inside the RIE chamber also lets some amount of chromium (directly available on surface) to diffuse into the surface which is impossible to remove later. However, for applications other than the ones involving electrical control, such a mask can be very efficient.

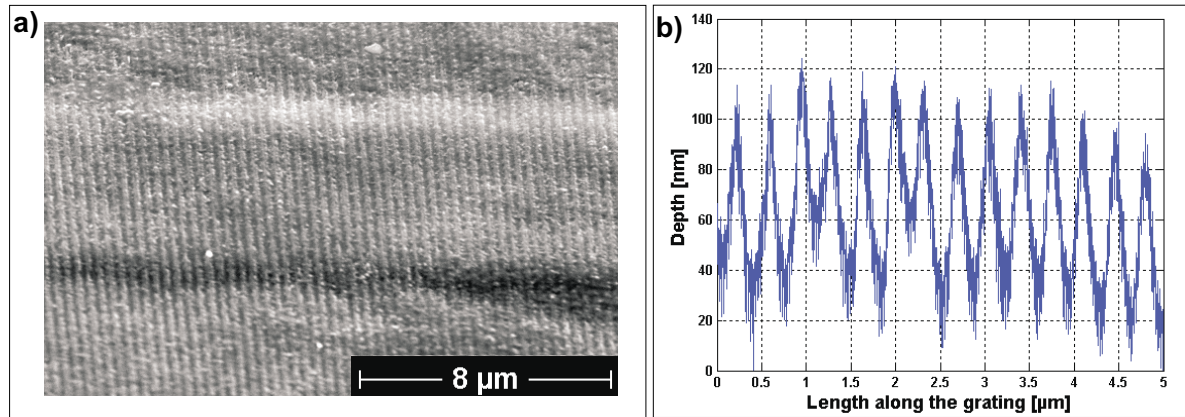


Figure 5.22: Corrugated  $Ti:LiNbO_3$  waveguide. a) Scanning electron micrograph of dry etched grating in the waveguide and b) atomic force microscopy (AFM) line scan along the grating vector.

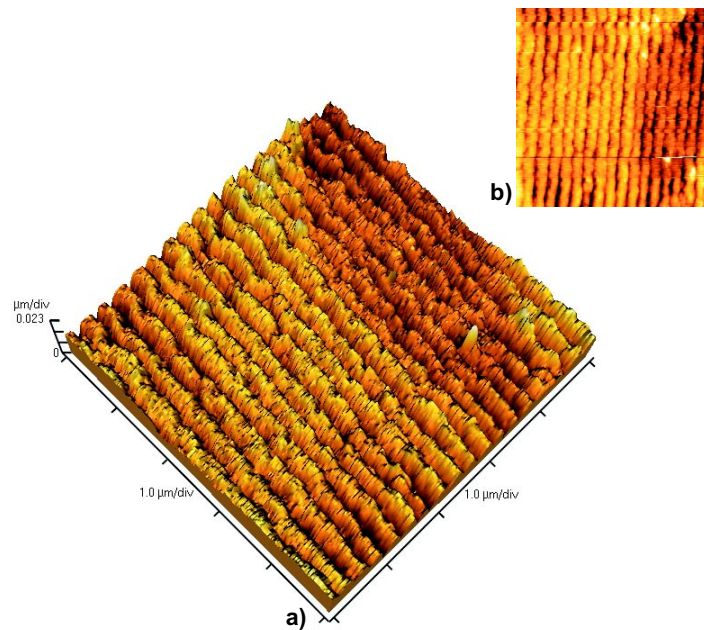


Figure 5.23: Surface-relief grating in  $Ti:LiNbO_3$  waveguide. a) 3D AFM scan of the corrugated grating and b) 2D AFM scan of the grating.

So, I finally used the mask prepared with shadow evaporation due to the concern of electrical short circuiting with the direct metal mask on the crystal as discussed above. The crystal with the mask was then exposed to RIE with  $\text{SF}_6$  which was done at Institut für Hochfrequenz (IHF) technik, TU Darmstadt. The parameters of the etching had to be optimized at first. This was done with the numbers available from literature for the etch rate of lithium niobate with  $\text{SF}_6$  and with few initial trials of etching and checking the etched height with an  $\alpha$ -stepper. RIE was finally done at an RF-power of 200 Watt, chamber pressure of 125 mTorr, DC-bias voltage of 100 V, gas-flow rate of 75 sccm/min for 20 minutes. Another important point to mention here is that the substrate was short-circuited or grounded inside the ion chamber by putting some conductive silver paste between the crystal edges and the metallic crystal holder.  $\text{LiNbO}_3$  is not a pure dielectric material (like glass) and has certain impurities and thus has free mobile charges (electrons and ions). When exposed to ion beam inside the chamber,  $\text{LiNbO}_3$  builds up a surface charge layer which deflects the ion beam away from the surface and thus the etching is not effectively done and has to be done for much longer duration. Grounding or shorting the crystal with a conductive silver paste provided the simple solution. After etching, the residual chromium and resist was removed using chromium etchant and other liquid solvents such as acetone and iso-propanol. The sample was then examined with SEM and AFM as shown in Fig. 5.22 and Fig. 5.23. The grating depth could be varied by changing the thickness of chromium layer and the etching time. The coupling coefficient depends on the grating depth and as already discussed, the required grating depth for near total reflection and for an about 8-10 mm long grating in  $\text{Ti:LiNbO}_3$  waveguide should be  $\approx 150$  nm. Considering the apodization effect, this depth should be more for a given grating length.

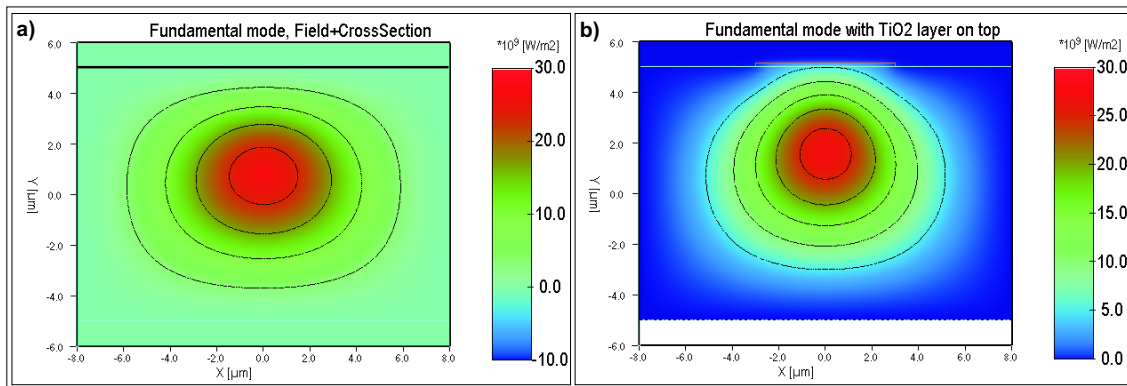


Figure 5.24: Modal field distribution in the waveguide: a) without any cover and b) with 20 nm  $\text{TiO}_2$  cover film on top of the waveguide (straight line at  $y = 5 \mu\text{m}$  represents the top edge of the waveguide).

In the next step, copper electrodes were deposited on both sides of the waveguide. The waveguide grating was then covered with a 20 nm  $\text{TiO}_2$  layer in order to allow the modal field to efficiently interact with the grating etched in the upper part of the waveguide. As seen in Fig. 5.24, the modal field is pulled up in the waveguide region due to the presence

of a layer with higher refractive index. The whole surface was then covered with a silica protective layer, single-mode fiber pigtailed were attached on both ends of the waveguide and the crystal was packed in a protective cover.

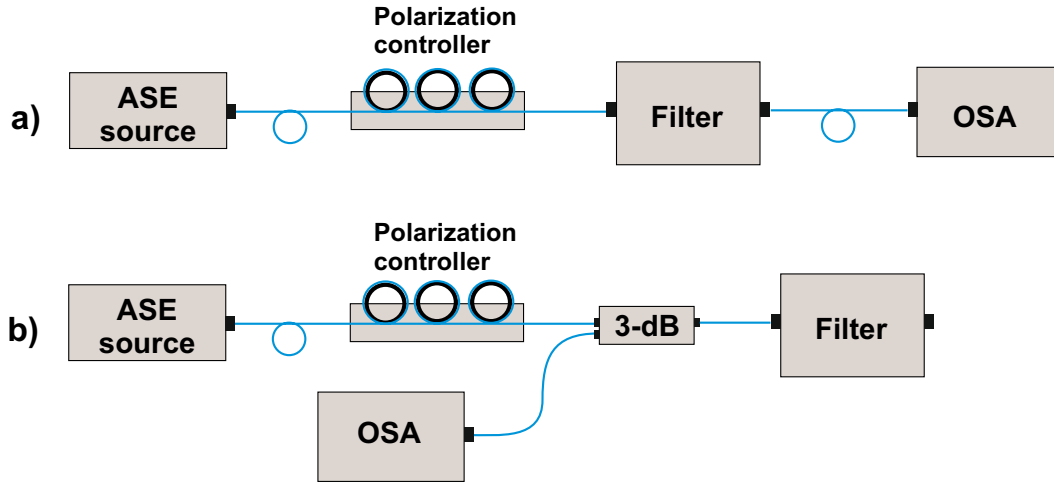


Figure 5.25: Measurement set-up for characterization of the grating filter: a) transmission measurement set-up and b) reflection measurement set-up.

### Measurements with the fabricated Grating Filter

The fabricated and packaged grating filter was then examined for its transfer function and electrical control. Fig. 5.25(a) and (b) illustrate the measurement set-ups in transmission and reflection, respectively. For measuring the transmission and reflection spectrum, output from a broadband source based on erbium doped fiber amplifier with amplified stimulated emission (ASE) was coupled to the filter via an optical fiber patch-cable. The transmission spectrum of the source is shown in Fig. 5.26(a). A polarization controller was inserted in order to choose the right polarization to enter the waveguide. The output from the filter was coupled to a grating-based optical spectrum analyzer (OSA). For reflection measurements, a 3-dB single-mode fused fiber coupler was used as shown in Fig. 5.25(b). The transfer function of the polarization controller was determined with respect to the angle of the circular IR-polarizer axis for different orientation of the loops. One of the transfer functions for a fixed orientation of the loops is shown in Fig. 5.26(b).

The measured transfer function of the grating filter in transmission and reflection is shown in Fig. 5.27. The dip seen on the left (shorter wavelength) side at around 1554 nm of the spectral transfer function is due to the coupling to radiation or cladding modes and appears due to a slight tilt of the grating with respect to the waveguide. If the device symmetry is assured, this dip should not be observed. The device, however, has considerable insertion loss due to misalignment between the attached fiber pigtailed and the waveguide ends and

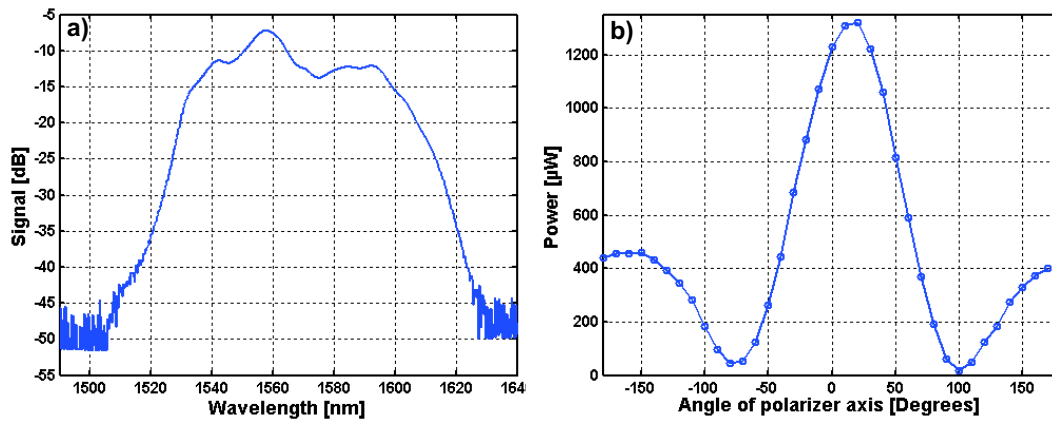


Figure 5.26: a) Transmission spectrum of the used broadband ASE source and b) transfer function of the polarization controller for a fixed orientation of the loops.

also due to absorption loss (relatively little) in the waveguide. The insertion loss can be reduced by ensuring better alignment between the fiber pigtails and the waveguide ends.

The central reflected wavelength of the filter is 1554.47 nm and spectral bandwidth (FWHM) is 0.18 nm. The filter can be designed for the entire L- and C- band of the optical communication systems by changing the angle between the interfering beams used for patterning the photoresist grating. Such filters can be used in add-drop multiplexers for telecommunications. For dropping multiple wavelengths, multiple grating filters can be used in series. Fig. 5.28 shows the transfer function of two such filters used in series. The slope seen in the measurement is due to the broadband source which has relatively more power near

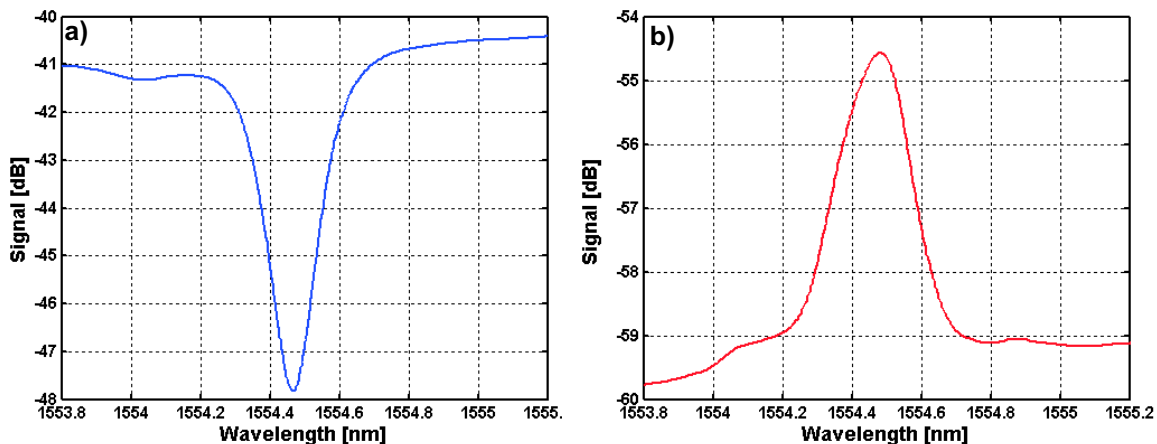


Figure 5.27: Measured transfer function: a) in transmission and b) in reflection.

1555 nm than near 1550 nm as can be seen in Fig. 5.26(a). One of the filter had a weaker grating with a phase jump and thus the diffraction efficiency is lower and two dips appear in the transfer function. This is a demonstration of an add-drop filter which can drop three different wavelengths. However, an array of such waveguide gratings with different central reflection wavelengths, fabricated on the same substrate can make an efficient wavelength demultiplexer.

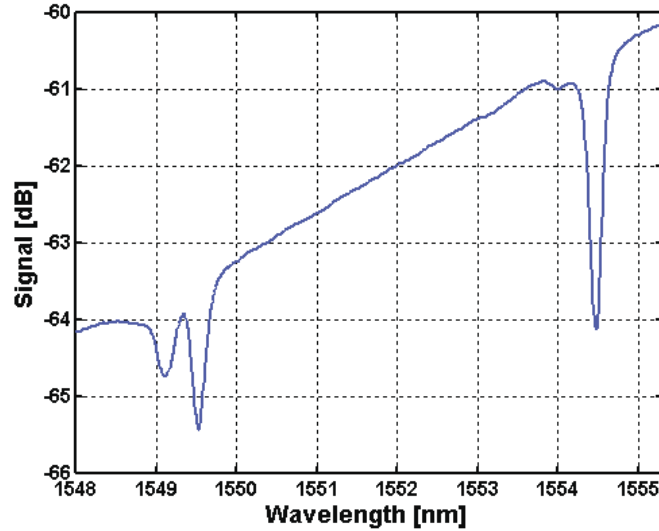


Figure 5.28: Measured transfer function of two grating filters connected in series.

For more accurate measurements of the grating filters with narrow-bandwidth, the ASE source (broadband source) was replaced by a tunable IR laser (narrowband source) and the OSA (narrowband detector) was replaced by a photodetector (broadband detector). The measurements done with the OSA are limited by the resolution of grating of the OSA. On the other hand, a very narrow bandwidth source like laser provides a much more precise measurement of the spectrum. The transfer function as measured with the tunable IR laser and photodetector controlled with a Labview program is shown in Fig. 5.29(a). The measured function is compared to the simulated function calculated using Kogelnik's theory. Although the theoretical fit matches well at the peak, the side lobes are not well resolved in the measured plot. This can be attributed to some phase errors in the grating occurred at the time of fabrication. In comparison to the measurements done with broadband source and the OSA, here the sidelobes are better resolved and the central peak is narrower (FWHM = 0.16 nm) due to the narrow bandwidth laser used for the measurement. Though the measured data shows some steps which is due to the step tuning of the laser, the measurement matches quiet well to the theoretical prediction.

In the next measurement step, a dc voltage was applied to the electrodes in order to change the effective index in the waveguide region which in turn leads to a change in the

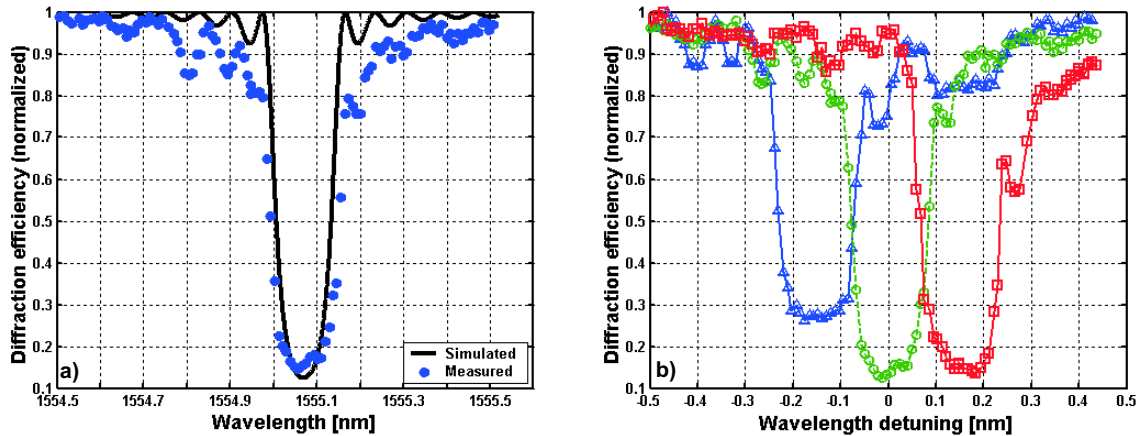


Figure 5.29: a) Measured transfer function of the grating filter as compared to the simulated function and b) electrical tuning of the filter transfer function-  $\Delta$ :  $E = +10 \text{ V}/\mu\text{m}$ ;  $\circ$ :  $E = 0$ ;  $\square$ :  $E = -10 \text{ V}/\mu\text{m}$ .

central reflected (diffracted) wavelength. As discussed earlier, continuous tuning of the dc voltages leads to a continuous change in the effective refractive index and hence leads to a continuous tuning of the filtered wavelength. The spectral transfer function of the filter was measured before and after the application of the control voltage. As discussed in chapter 4, positive and negative polarity of the applied voltage leads to decrease or increase in the refractive index (via Electro-optic effect) depending upon the orientation of the crystal and the polarization of the incident light. Therefore, both the polarities of the applied dc voltage could be used to tune the filtered wavelength in opposite directions as shown in Fig. 5.29(b). It can be seen that the width of the spectrum (reflection bandwidth) is about 0.17 nm and the shift of the spectral transfer function for the applied field of  $10 \text{ V}/\mu\text{m}$  is 0.15 nm. These values are in satisfactory agreement with the theory. With higher applied voltages, the transfer function can be shifted further. The experiments have shown that a continuous tuning of the central wavelength in the  $\pm 0.3 \text{ nm}$  range with a maximum applied field of  $\pm 10 \text{ V}/\mu\text{m}$  can be achieved. The maximum value of the applied voltage is, however, limited by the breakdown voltage. By further optimization of the crystal and waveguide orientation and the design and configuration of electrodes, it is possible to improve the working parameters considerably.

The results presented in this section, in general, verify the implementation of the electrical control of diffraction from fixed (corrugated) gratings in waveguide and demonstrate the principle of real-time electrical tuning of the spectral transfer function of a fixed grating based filter. However, such narrow-bandwidth (0.17 nm) filter with fixed grating, central wavelength near 1550 nm and continuous electrical tuning of the peak wavelength are very promising for telecommunication applications. The integrated optical implementation makes it more promising for telecommunications as the filter can be directly placed in